Sustainable Energy & Fuels

ROYAL SOCIETY OF CHEMISTRY

PAPER

View Article Online
View Journal | View Issue

Cite this: *Sustainable Energy Fuels*, 2026, **10**, 1135

Phosphorous containing inverse vulcanised sulfur polymers as Li–sulfur positive electrodes

Haoran Wang,†[ab] Pan Yang,†[ab] Alex R. Neale,[ab] Liam J. Dodd,[a] Peiyao Yan,[a] Bowen Zhang,[a] Laurence J. Hardwick *[ab] and Tom Hasell *[ab]

Received 17th January 2026
Accepted 27th January 2026

DOI: 10.1039/d6se00065g

rsc.li/sustainable-energy

The synthesis and electrochemical evaluation of ternary sulfur – diphenyl(4-vinylphenyl) phosphine – dicyclopentadiene (SPD) polymers is reported. Polymers with a homogenous particle size around 80 nm were prepared by inverse vulcanisation and anti-solvent precipitation methods. The nanoparticulate polymer led to a uniform morphology of the electrode and high accessibility of the electrochemically active sulfur leading to a specific capacity of 1436 mAh g_s^{-1} and improved cycling stability, relative to comparative samples prepared at micrometre scale.

Introduction

The lithium–sulfur (Li–S) battery is considered as a promising alternative to the lithium-ion system for energy storage devices in the future because of its theoretically high specific capacity (1672 mAh g_s^{-1}) and specific energy (2600 Wh kg^{-1}).[1,2] However, the commercialisation of the Li–S chemistry has been hindered so far by relatively poor cycling performance. This can be attributed to the limitations of the sulfur-based cathode, owing to the insulating property of sulfur and its reduced solid product lithium sulfide (Li_2S). Additionally, a serious volume expansion in S-electrode structure occurs during cycling resulting from the density disparity between sulfur and Li_2S.[3,4] Moreover the "shuttle effect" whereby soluble polysulfide intermediate migrate and react at the lithium metal electrode which results in the incomplete use of the active sulfur and shortening the lifetime of Li–S cells.[5] Researchers have proposed several strategies to address the shuttle effect, such as physical confinement and chemical confinement of long-chain polysulfides,[6–9] liquid–solid reductive reaction acceleration by catalysis, and through chemically locking in the sulfur into an organic polymeric chain, *via* inverse vulcanisation.[10–12]

An inverse vulcanised polymer with relatively high sulfur content was first reported as an organosulfur cathode material in 2013.[12] The introduction of active sites within the polymeric structure of crosslinked sulfur polymers were reported to enhance the chemical affinity to high-order polysulfide intermediates. This implementation of chemical confinement strategy led to comparable long-term charge–discharge stability, when compared to well-designed host materials.[13] Considering the facile inverse vulcanisation method and potential for large-scale preparation, the resultant polymeric materials exhibit certain advantages towards practical application. Regarding the exploration of active sites in the organic moieties of inverse vulcanised polymers, the main strategy is to design nucleophilic or electrophilic moieties that can chemically anchor Li or sulfur-chains, respectively, within the intermediate lithium polysulfides. Recently, crosslinking monomers with various heteroatoms such as O, S and N have been widely investigated in inverse vulcanisation to generate electroactive functional polymers, delivering promising results for fabricating high-performance Li–S cells.[14–16] There is insufficient research in the evaluation of crosslinkers containing phosphorous heteroatoms that can provide further binding sites to polysulfides, thus introducing a further chemical trap to limit S dissolution. Additionally, although several methods have been proposed to produce inverse vulcanised polymers at the nanoscale,[17,18] the size impact of polymeric nanoparticles on electrochemical behaviour of Li–S cells has been seldom reported.

Herein, the monomer diphenyl(4-vinylphenyl) phosphine (D4VPP) with a P heteroatom bonded to three aromatic branches was employed as functional crosslinker in inverse vulcanisation. Dicyclopentadiene (DCPD) was also utilised as a secondary crosslinker for stabilising high sulfur content. Polymeric nanoparticles with homogeneous average size around 80 nm were obtained by anti-solvent precipitation and investigated for their electrochemical properties as a Li-sulfur positive electrode.

Experimental

Synthesis of sulfur – diphenyl(4-vinylphenyl) phosphine – dicyclopentadiene samples

Sulfur – diphenyl(4-vinylphenyl) phosphine – dicyclopentadiene (SPD) polymer was synthesised by inverse vulcanisation. 4 g

[a]*Department of Chemistry, University of Liverpool, Oxford Street, Liverpool L69 7ZD, UK. E-mail: hardwick@liverpool.ac.uk; T.Hasell@liverpool.ac.uk*

[b]*Stephenson Institute for Renewable Energy, Department of Chemistry, University of Liverpool, Peach Street, Liverpool L69 7ZF, UK*

† These authors contributed equally to this work.

sulfur powder (Brenntag) was mixed with 0.5 g diphenyl(4-vinylphenyl) phosphine (D4VPP) (Sigma Aldrich, 97%) and 0.5 g dicyclopentadiene (DCPD) (Sigma Aldrich, >96%) crosslinkers (mass ratio 8 : 1 : 1) in a 14 mL glass vial. All reactions were carried out in open air. The mixture was then heated to 140 °C until complete melting of sulfur had occurred. The reaction proceeded with 900 rpm stirring for *ca.* 12 min at 180 °C. The resulting viscous sample was cured at 140 °C in an oven for 24 h to obtain a crosslinked polymer. Finally, the rigid polymer was ground into fine powder by ball milling for 3 h (denoted as SPD1).

For anti-solvent precipitation, 1.5 g of the ball milled SPD1 was dispersed in 6 mL tetrahydrofuran (THF) and the suspension was stirred for 24 h. Subsequently, the suspension was filtered into two parts. The filtrate THF solution with a partial soluble polymer fraction was added dropwise into 60 mL deionised water with vigorous stirring. SPD nanoparticles (denoted as SPD2) were obtained by this anti-solvent precipitation method, which were collected by evaporating most of the water at room temperature before vacuum drying for 24 h. The precipitate, which had been insoluble in THF, was collected and vacuum dried for 24 h (denoted as SPD3) (Fig. S1a). The SPD2 nanoparticles were white in colour, whilst both SPD1 and SPD3 were dark brown in appearance (Fig. S1b).

To determine the chemical environment of P atoms during inverse vulcanisation, D4VPP monomer was reacted with a lower amount of elemental sulfur independently (D4VPP : S = 2 : 1 in mass ratio). The heating temperature was controlled to 180 °C with the reaction period up to 1 h. After 24 h curing under 140 °C, the polymer was ground into powder using a rotary grinder, and the product designated as SD4VPP. Moreover sulfur- and oxygen-containing model compounds D4VPP-S and D4VPP-O were synthesised, and the corresponding sulfur-rich polymers, SD4VPP-S and SD4VPP-O were prepared, under identical reaction conditions with SD4VPP.

Characterisation

Powder X-ray diffraction (PXRD) patterns of SPD polymers were obtained using a PANalytical X'Pert PRO diffractometer with Cu-Kα radiation. Differential scanning calorimetry (DSC) curves were collected by Q2000 DSC (TA instruments) under N_2 with a heating rate of 10 °C min^{-1}. The morphology of SPD polymers and electrodes were observed by Hitachi S-4800 cold-field emission scanning electron microscope (SEM). The N_2 adsorption/desorption isotherm was conducted with Micrometric 3-Flex 3500 gas sorption analyser using the Brunauer–Emmett–Teller (BET) method. The particle size of SPD2 was obtained by dynamic light scattering (DLS) analysis using Malvern Panalytical Zetasizer Nano Particle Sizer. Nuclear magnetic resonance (NMR) spectra of monomers and polymers were tested by a Bruker Advance DRX (400 MHz) spectrometer with dimethyl sulfoxide-d_6 as solvent. Fourier transform infrared (FTIR) spectra were collected between 400–4000 cm^{-1} (Bruker Vertex 70). CHNS element analysis was conducted *via* Vario Micro cube elemental analysers. High-performance liquid chromatography (HPLC) test was performed by 1260 MD-HPLC System (Agilent) with the elution combined with 5% water and 95% methanol. Thermal gravimetric analysis (TGA) data was recorded by Q5000IR analyser (TA instruments) under N_2 with an automated vertical overhead thermobalance. The test program was optimised to ramp to 350 °C followed by an isothermal step for 1 h to eliminate possible interference from degradation of crosslinkers. Ultraviolet-visible (UV-vis) spectra of liquid samples were obtained by Cary 5000 UV-vis-NIR Spectrometer.

Li_2S_6 adsorption test

The Li_2S_6 solution was obtained by stirring Li_2S (46 mg) and elemental sulfur (160 mg) in 20 mL 1,2-dimethoxyethane/1,3-dioxolane (DME/DOL) solvent (1 : 1 vol : vol) at 65 °C under Ar atmosphere for 24 hours. This mixture was then diluted to 1 mM for the subsequent test. Therein, 15 mg SPD samples were added into 2 mL of both the Li_2S_6 solution and pristine DME/DOL solvent mixture. UV-vis data in the range of 700–230 nm was collected for DME/DOL solvent and Li_2S_6 solution before and 24 h after the addition of SPD samples to evaluate their chemical confinement ability to long-chain polysulfides.

Electrochemical measurements

In the slurry preparation, the SPD samples were combined with conductive carbon material (acetylene black, Sigma Aldrich) and poly (vinylidene fluoride) (Kynar PVDF, Arkema) binder in a mass ratio of 6 : 3 : 1 (100 mg total mass). The mixture was then manually ground by mortar and pestle for 15 minutes and collected into a vial with the addition of *ca.* 0.3 mL anhydrous *N*-methyl-2-pyrrolidone (NMP). The slurry stirred for 24 h and then uniformly coated on aluminium foil by doctor-blade. The electrode cast was then dried under vacuum at 60 °C for 18 h. Positive electrode discs (10 mm diameter) were punched out and dried under vacuum at 60 °C for 18 h and then transferred into the Ar-filled glovebox (H_2O, $O_2 \leq 0.1$ ppm). The active sulfur loading within all positive electrodes was controlled in the range of 1.4–1.6 mg_s cm^{-2}. In the glove box, the positive electrode was assembled into coin cells with a polished lithium foil disc (12 mm diameter, 0.38 mm thickness) as counter/reference electrode, a glass microfibre separator (Whatman GF/F, 16 mm diameter) and electrolyte (1.0 M lithium bis(trifluoromethanesulfonyl)imide (LiTFSI) in DME : DOL = 1 : 1 vol:vol with 1% $LiNO_3$). The ratio of electrolyte volume to active sulfur mass was controlled to 30 μL mg_s^{-1}.

All electrochemical measurements were conducted at 30 °C after a rest period of 18 h. Cyclic voltammetry (CV) was measured using an MPG-2 workstation (Biologic) within the potential range of 1.5–3.0 V *vs.* Li^+/Li. The current densities in CV curves and specific capacities were normalised based on the mass of active sulfur. The galvanostatic discharge–charge cycling was performed using Maccor Series 4000 and LAND CT3001A battery cyclers between 1.5–2.8 V *vs.* Li^+/Li at various C-rates (where 1C = 1672 mAh g_s^{-1}, derived from the theoretical capacity of S). One discharge–charge cycle was completed after the 18 h rest, and then the 1st discharge–charge cycle was recorded. Electrochemical impedance spectroscopy (EIS) was

measured at open circuit potential in the frequency range from 1 MHz to 0.01 Hz with 10 mV amplitude after the 1st, 100th and 200th discharge–charge cycle as well as another 18 h rest by VSP workstation (Biologic).

Computational simulation

Density functional theory (DFT) calculations were performed in the gas phase, on structures that were initially geometry optimised with Merck molecular force field (MMFF) molecular mechanics. Further geometry optimisation and energy calculation were performed in the Gaussian 09 program package, using the BP86 functional, combined with the 6-311+G (2df, 2p) basis set and a GD3(BJ) empirical dispersion correction. Electrostatic potential maps were generated in Avogadro 2 software.

Results and discussion

Materials characterisation

PXRD patterns of crystalline sulfur (S_8) and sulfur – diphenyl(4-vinylphenyl) phosphine – dicyclopentadiene (SPD) samples, SPD1 (inverse vulcanisation with DCPD and D4VPP monomers), SPD2 (anti-solvent soluble precipitate) and SPD3 (anti-solvent insoluble precipitate) are shown in Fig. 1a. All samples exhibit broad peaks in the region of 12–32° due to the amorphous nature of the polymeric structure. For SPD1, no unreacted crystalline sulfur can be observed in the polymer structure from the absence of crystalline sulfur reflections within the PXRD pattern. However, both SPD2 and SPD3 samples display reflections located at around 23°, implying a residual amount of crystalline sulfur and due to depolymerisation during anti-solvent procedure. DSC probed the degree of polymer crosslinking from the glass transition temperature (T_g). Apparently, compared with initial SPD1 (24.9 °C), SPD2 possesses a dramatically decreased T_g (3.2 °C) while SPD3 shows a similar one of 30.5 °C (Fig. 1c). These results confirm a lower degree of crosslinking for SPD2 than for SPD1 and SPD3, that concurs with the synthesis procedure whereby the SPD2 fraction is solubilised in in THF. Additionally, there is a further T_g in all three SPD samples at 130 °C, resulting from a minor fraction of phase separated S-DCPD domains in the SPD samples, suggesting the effective function from DCPD monomer in this ternary system of enhancing crosslinking degree and stabilizing a high content of sulfur.[19]

To monitor the reaction of the C=C bonds of the monomers in the polymerisation reaction, the SPD-based polymers were characterised by NMR. The shifts at 5.30, 5.87 ppm can be assigned to C=CH_2 and 6.73 ppm from CH=C in D4VPP and 5.95 and 5.48 ppm from the protons of norbornene C=C bonds in DCPD, but these peaks are absent in the spectra of the polymer samples (Fig. 1d).[20,21] Therefore, the C=C bonds of both monomers have been sufficiently converted during inverse vulcanisation. Additionally, the peaks of the aromatic protons (7.15–7.53 ppm) shift slightly downfield. A shift of the phosphorus signal from −5.84 to 42.85 ppm was observed in the ^{31}P spectrum in Fig. 2a, indicating the change of P chemical environment for D4VPP after the reaction, which would be consistent with a change to higher oxidation state. To further understand the evolution of the P environments in the polymers, a binary polymer consisting of only S and D4VPP was prepared for NMR analysis. Based on the results of ^{1}H, ^{31}P and ^{13}C spectra (Fig. 2b–d) both aromatic proton and phosphorus become more de-shielded (weakly for H and strongly for P), suggesting an electron withdrawing group generated on the P bonded to three benzene branches. According to literature, the oxidation of P atoms has been proposed under heating in air.[22,23] However, in a sulfur-rich environment, phosphorus (P) may undergo sulfurisation to form P=S bonds. To elucidate the specific bonding environment of phosphorus atoms in the polymer SPD, the molecular model compounds D4VPP-O and D4VPP-S, as well as the corresponding sulfur-containing polymers SD4VPP-O and SD4VPP-S were synthesised under identical experimental conditions. Detailed characterisation data, including ^{1}H NMR, ^{13}C NMR, ^{31}P NMR spectra and CI-MS, are shown in Fig. S2–S13. The ^{31}P NMR spectrum of the oxygen-containing monomer shows a characteristic P=O resonance at 28.91 ppm. After reaction with elemental sulfur, this signal remains essentially unchanged, and phosphorus in the polymer SD4VPP-O still appears at 28.91 ppm, indicating that the P=O bond was not affected by sulfur under these conditions. In contrast, the ^{31}P NMR spectrum of D4VPP-S exhibits a resonance at 42.89 ppm, which can be assigned to the P=S bond. Notably, the phosphorus signal in the corresponding polymer SD4VPP-S remains at 42.89 ppm, identical to that observed in the polymer SPD synthesised in this work. These results collectively demonstrate that, after the reaction of D4VPP with elemental sulfur, phosphorus is sulfurised to form P=S bonds in a sulfur-rich environment. Comparison between the NMR results at 2 minutes and the spectra of the sulfurised monomer with P=S bond show considerable consistency both in ^{1}H and ^{13}C spectra,[24,25] indicating the formation of a P=S bond in the monomeric structure at the initial stage of the inverse vulcanisation process.

To further determine the covalent nature of SPD1, SPD2 and SPD3, FTIR spectra of the two monomers, SD4VPP and SPD samples are presented Fig. 1e and S14. For DCPD, the peaks at 3045 and 1338 cm^{-1} are ascribed to stretching and bending vibrations of C=C–H, respectively.[21] The characteristic peak at 916 cm^{-1} corresponds to vinyl C=C bond in D4VPP,[26] while the bands at 1431 and 694 cm^{-1} could be attributed to vibration of P–C (aromatic) bond and symmetric vibration of P–C bond, respectively.[27] After inverse vulcanisation, the signal from C=C bond in D4VPP at 916 cm^{-1} disappears in the spectra of both SD4VPP and SPD samples, which demonstrates full consumption of these double bonds in the reaction. Additionally, a newly observed band at 671 cm^{-1} corresponding to the C–S bond,[28] proves the combination between sulfur chain and crosslinkers. A sharp characteristic peak located at 1101 cm^{-1}, not shown in the spectra of both monomers, arises when testing all polymers. This is due to the vibration of P=S bond, which reveals the sulfurisation of P atom in D4VPP monomer.[29,30] Furthermore, the FTIR bands resulting from P-aromatic C bonds in D4VPP show negligible difference in all polymers, suggesting the stability of its organic structure (P atom bonded to 3 branches)

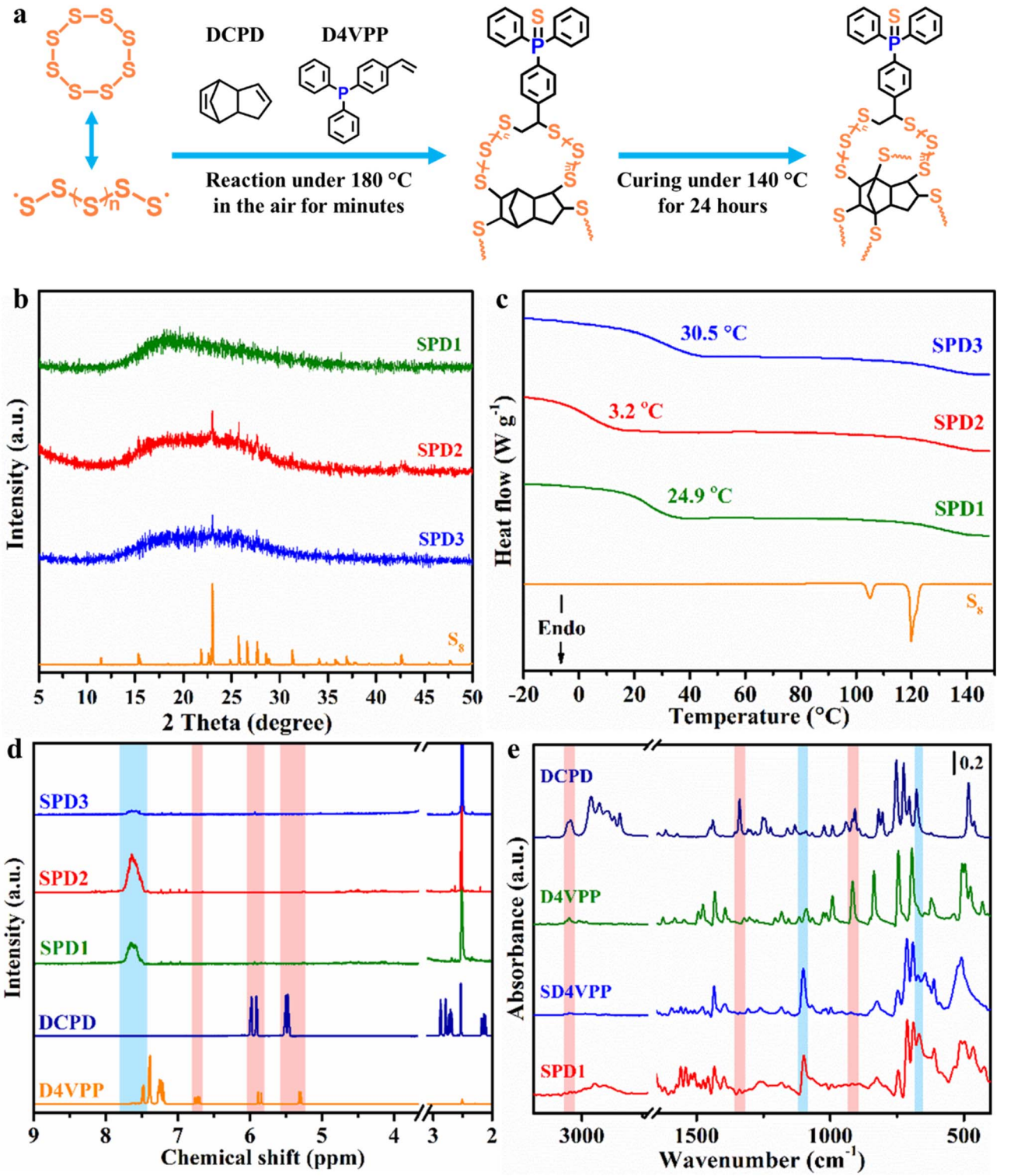

Fig. 1 (a) Synthetic scheme for sulfur – diphenyl(4-vinylphenyl) phosphine – dicyclopentadiene (SPD) polymer *via* inverse vulcanisation. (b) PXRD patterns and (c) DSC curves of elemental sulfur (S_8) and SPD samples. (d) ^{1}H NMR spectra of diphenyl(4-vinylphenyl) phosphine (D4VPP), dicyclopentadiene (DCPD) monomers and SPD polymers. (e) FTIR spectra of D4VPP, DCPD monomers and SD4VPP and SPD1 samples.

after both inverse vulcanisation and anti-solvent precipitation. The scheme in Fig. 1a demonstrates the structure of SPD polymer during synthesis according to the above discussion. DCPD molecules may be converted to cyclopentadiene (CPD) under high temperature.[31,32] However, considering the low boiling point (40.8 °C) of CPD and the previous solid-state NMR results of the SDCPD polymer prepared by a similar method,[21] the rigid

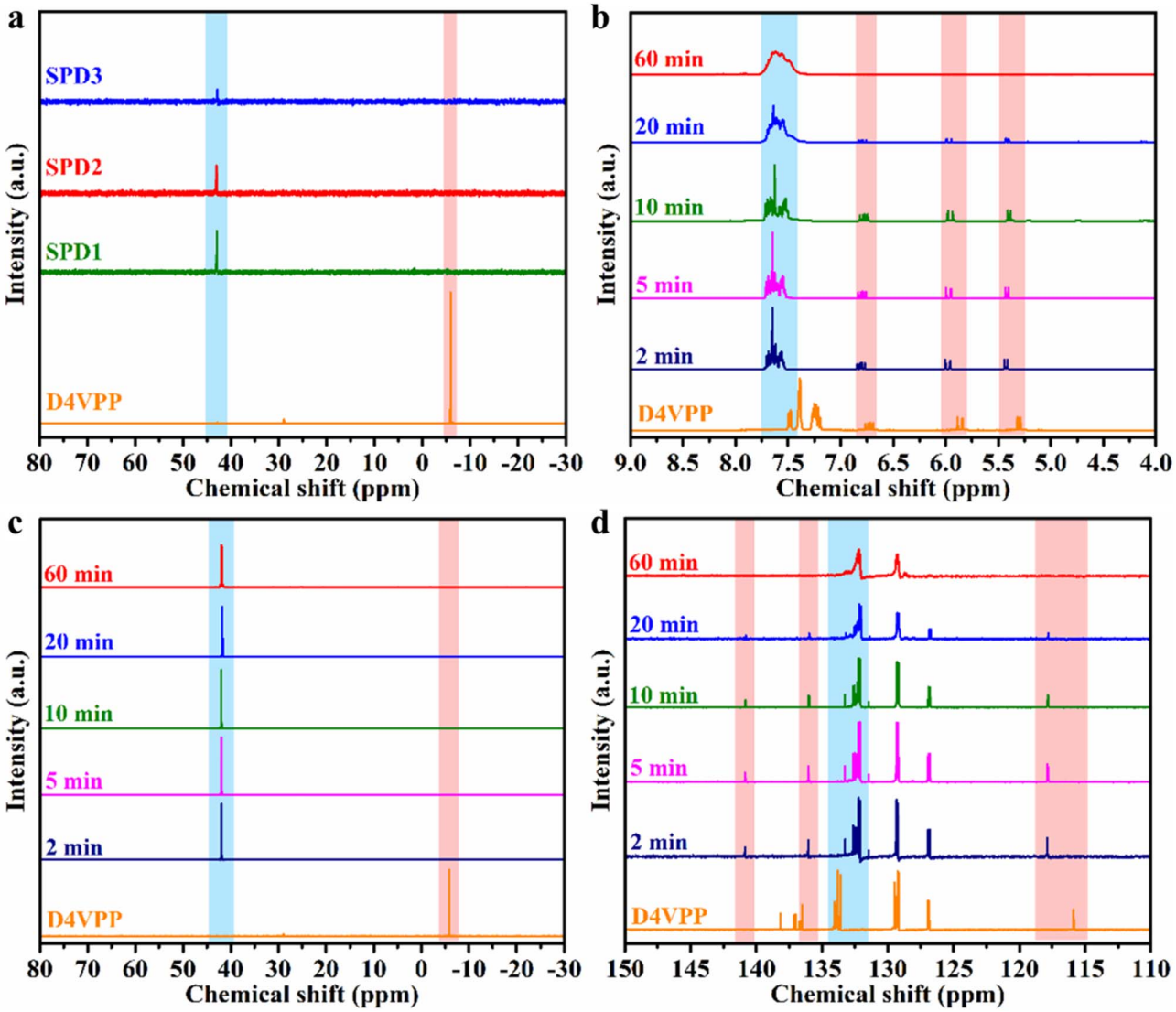

Fig. 2 (a) ^{31}P NMR spectra of SPD samples. (b) ^{1}H, (c) ^{31}P and (d) ^{13}C NMR spectra of the specimens at different times during the inverse vulcanisation between sulfur and D4VPP monomer. The structural change of D4VPP has been achieved during the initial two minutes of heating. This does not affect the subsequent sulfur radical attack to C=C bonds as the chemical shifts of aromatic proton and phosphorus signals at this moment have been consistent with all SPD-based polymers. Then, the C=C bonds start to react with sulfur radicals after 10 min heating and complete the reaction at 1 h, which further corroborates the reactivity of C=C bonds from D4VPP monomer.

polymeric backbone of the prepared samples here is shown to be based on DCPD rather than CPD.

SEM shows the morphology of the three SPD polymer samples (Fig. 3). For SPD1, the powder size was 5 μm (Fig. 3a and b). The morphology of SPD2 into nanosphere array with anti-solvent precipitation (Fig. 3c and d). The average diameter of single nano-sphere from SEM images is approximately 80 nm and DLS analysis indicates that most particles are in the range of 60–90 nm (Fig. S15). SPD3 (Fig. 3e and f) shows slightly larger size of about 10 μm. The N_2 adsorption/desorption isotherms in Fig. S16 indicate the morphological difference among the SPD samples before and after anti-solvent precipitation. SPD1 and SPD3 both show negligible adsorption/desorption response due to the similarly large (micrometre) particle size, and the absence of pores. However, the curve from SPD2 demonstrates adsorption/desorption at high relative pressure, consistent with microporosity, with a BET surface area of 4.8 $m^2\ g^{-1}$ (Table S1). This is likely to be the result of interparticle voids caused by packing together of the nanoparticles. In addition, the nano-scale particle size of SPD2 is expected to provide a larger accessible surface area, which facilitates more effective inter-facial contact between the active sulfur species and the carbon black conductive additive (Fig. S17). Such improved physical contact is beneficial for electron transport and contributes to the enhanced electrochemical performance.

Elemental analysis tests for CHNS contents were conducted for SPD1-3. All three samples show approximately 80% sulfur content, close to the calculated ratio (Table S2). Among the samples, SPD2 possesses the highest sulfur proportion, which could be explained by its relative lack of the crosslinkers,

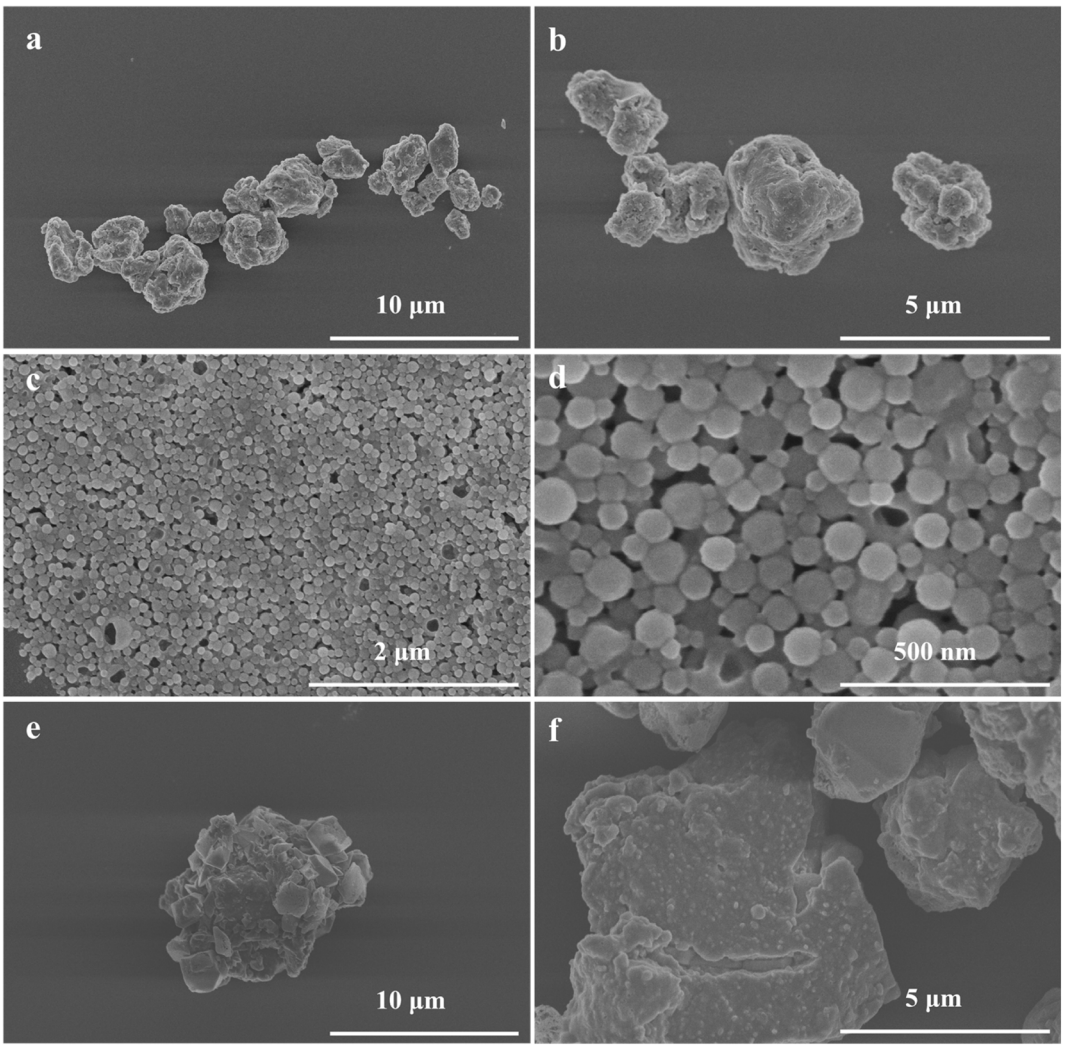

Fig. 3 SEM images of (a and b) SPD1 (ball milled), (c and d) SPD2 (antisolvent precipitated soluble filtrate) and (e and f) SPD3 insoluble precipitate powder.

considering the lower ratio of carbon. Therefore, SPD2 is supposed to contain longer average sulfur rank in its polymeric structure and lower crosslink degree, as evidenced by its low T_g and solubility in THF. SPD3 with higher T_g, as the opposite of SPD2, contains more carbon and less sulfur compared with SPD1. All samples contain a lower proportion of S, C, and H than would be expected from products formed from the reaction of the un-sulfurised phosphorous monomer. This reduction in the proportion of detected elements could be attributed to the sulfurisation of the phosphorous to form P═S bonds, thereby increasing the mass ratio of undetected elements. Meanwhile, increase in the C/H ratio is exhibited among all samples, indicating the inverse vulcanisation reaction suffers leads to limited hydrogen abstraction and H_2S generation. It is possible there could be some amorphous sulfur component in the SPD samples, confined by the polymeric structure.[33] HPLC was used to detect amorphous sulfur by comparing their integration area with standard sulfur sample (Fig. S18a and Table S3). According to the results, SPD1 possesses around 10% amorphous sulfur (*i.e.*, no crystalline reflections were observed in the PXRD pattern, Fig. 1b). While for SPD2 and SPD3, the sulfur proportions here (*ca.* 11% and 6%, respectively) include both amorphous and crystalline sulfur compositions. Considering the potentially inactive nature of the sulfur atom on the C–S bond of polymers during electrochemical charge–discharge process,[34,35] the active sulfur content was determined by TGA characterisation. The results shown in Fig. S18b and Table S4 demonstrate that all SPD-based polymers have around 70% active sulfur, while the mass loss by 1.4% of SPD3 from 75 to 120 °C could be ascribed to slight residual THF or moisture.

In terms of safety and potential scalability of this reaction, it should be noted that the most problematic step is the synthesis of the polymers themselves. While this is straightforward at the scales performed here, as an exothermic bulk polymerisation it should be noted that there are risks of auto-acceleration if performed on larger scales. In such a case the heat generated by the reaction cannot escape sufficiently, leading to an increase in reaction temperature which as well as being dangerous itself can cause increased production of a toxic H_2S byproduct.[36] Despite these risks, scale-ups of inverse vulcanised polymers

have been successfully performed at kilogram scale[37] and beyond.[38]

Electrochemical performance

Electrochemical characterisation of the synthesised SPD polymers as the positive electrode is shown in Fig. 4. CV of the Li–S cells are presented in Fig. 4a. There are two similar reductive peaks in the range of 2.30–2.35 and 1.97–2.00 V for all SPD samples that could be ascribed to the formation of high-order soluble polysulfides (mainly S_6^{2-} and S_4^{2-}) and further low-order solid (Li_2S_2 and Li_2S) in sulfur reduction reaction, respectively. Correspondingly, two electrochemical processes ascribed to the oxidation of Li_2S_2 and Li_2S back to sulfur species could be observed by the peaks located at 2.28–2.45 V.[39,40] The reversible nature of the electrochemical reactions of SPD1-3 was shown by the repeatable CV curves across several cycles (Fig. S19). Meanwhile, the higher current density of the second cathodic peak of SPD2, compared with SPD1 and SPD3, demonstrates enhanced generation of short chain polysulfides. This suggests a potentially better discharge–charge performance from SPD2 because of the significant contribution to capacity from the liquid–solid conversion reaction.

Galvanostatic charge–discharge curves of the cells based on three SPD samples were firstly measured at 0.05C and the first cycle voltage profiles are illustrated in Fig. 4b. SDP2 delivers a specific capacity of 1436 mAh g_s^{-1} while SPD1 and SPD2 delivered slightly lower discharge capacities of 1200 and 1205 mAh g_s^{-1}, respectively. By comparing the potential gap (ΔE), calculated at the 50% DOD and SOC point, between charge and discharge platform, SPD2 (146 mV) and SPD3 (143 mV) appear to suffer less from internal polarisation than SPD1 (182 mV).[41] All voltage profiles feature two primary discharge plateaus corresponding to the two oxidation peaks observed in the CVs. These are denoted Q_1 and Q_2, respectively (labelled in Fig. 4b). The SPD2 electrodes exhibited higher specific capacity for Q_2 in contrast with SPD1 and SPD3 considering similar specific capacities for Q_1 for all SPD containing electrodes. Therein, discharge–charge curves at various C-rates of SPD polymers were recorded (Fig. S20) and the derived Q_2/Q_1 ratios are presented in Fig. 4c. SPD2 resulted in larger Q_2/Q_1 ratios than SPD1 and SPD3 under all tested C-rates in the range of 0.05–2C, consistent with the results of CV curves. This strongly supports the faster kinetics of the reductive process of liquid–solid conversion and further better discharge performance.[42,43]

The rate capability of the cells based on SPD polymers is presented in Fig. 4d where SPD2 exhibits the best rate performance among all samples. SPD2 delivers higher capacities at 0.05 and 0.1C of 1436 and 1200 mAh g_s^{-1} which fade during the five-cycle test as well as delivering stable specific capacities of around 1061, 940 and 719 mAh g_s^{-1} under 0.2, 0.5 and 1C, respectively. Significant fading in initial cycles was only observed in cells cycled at lower C-rate as reduced cell polarisation from these currents enabled maximum initial capacities to be obtained. Li–S cells were further evaluated for 500 cycles at 0.5C to examine the long-term stability and the results in Fig. 4e show reasonable cyclability of the three SPD samples. This

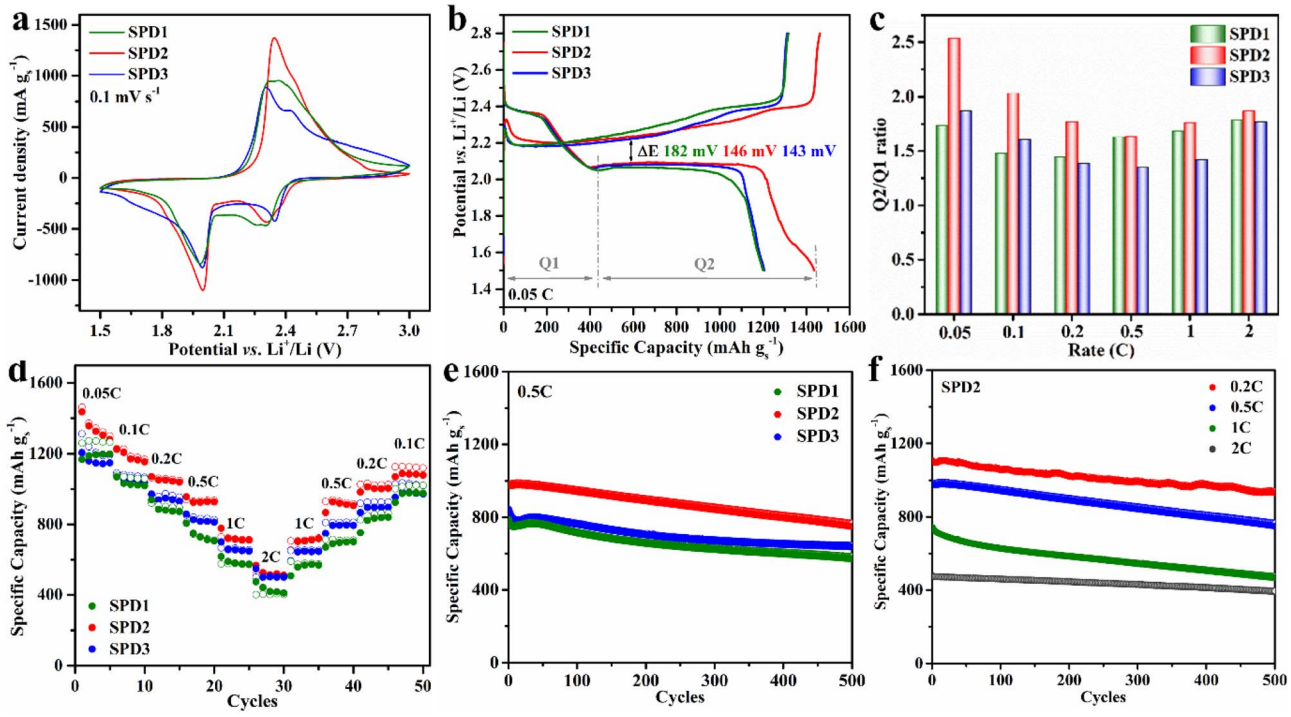

Fig. 4 Electrochemical performance of Li–S cells based on SPD electrodes with the sulfur loading in the range of 1.4–1.6 mg_s cm^{-2}. (a) The cyclic voltammetry curves with a scan rate of 0.1 mV s^{-1}. (b) The 1st discharge–charge curves at 0.05C. (c) Q_2/Q_1 values obtained from discharge curves under various C-rates from 0.05 to 2C. (d) The rate capability in the range of 0.05–2C. (e) The long-term test for 500 cycles under 0.5C. (f) The cyclability of the cells based on SPD2 under the C-rates from 0.2 to 2C.

result is significantly different from the long-term cycling performance of unmodified sulfur, for which a distinct capacity decay is typically observed during long-time cycling.[33,44,45] Specifically, for SPD2 at 0.5C, its specific capacity reaches 976 mAh g_s^{-1} in the 1st cycle and gradually decreased to 749 mAh g_s^{-1} (capacity retention 76.8%) at the end of the 500th cycle with a low performance decline of 0.046% per cycle. While for SPD1 (72.4%) and SPD3 (74.3%), the decay proportions under 0.5C are 0.055% and 0.051%, respectively. The slow cell degradation of all SPD polymers can be attributed to the alleviation of "shuttle effect" by strong chemical anchor effect to long chain polysulfides from the P═S bonds in polymeric structure, as discussed in detail above. The stable long lifetime of the cell based on SPD2 is further demonstrated by conducting the measurement for 500 cycles under different current density from 0.2 to 2C (Fig. 4f). Notably, the cell shows stable initial performance at higher C-rates (>0.2C) in Fig. 4f. Furthermore, the performance of the cells based on SPD2 with higher sulfur loadings (up to 3.8 mg_s cm^{-2}) was evaluated in Fig. S21, which demonstrates a stable capacity above 350 mAh g^{-1} for 200 cycles. The SPD2 material delivers a competitive cell performance compared with recently reported inverse vulcanised cathode materials in Table S5.

EIS measurements were conducted SPD1-3 containing cells after the 1st, 100th and 200th discharge–charge cycles. The resulting Nyquist plots are presented in Fig. 5. The first characteristic information is the high-frequency intercept of the *x*-axis, where the value of resistance mainly corresponds to the electrolyte resistance.[46] Notably, all cells suffer from the slight decrease of electrolyte conductivity after 200 cycles as some high-order polysulfides persist in the electrolyte rather than fully participate in the electrochemically process. This increased concentration of dissolved polysulfides raises the viscosity of the electrolyte and results in the increase of its resistance.[47] However, compared with our previous results using elemental sulfur-based electrodes in cell after long-term cycling, all the SPD electrodes undergo a lower rise in the electrolyte resistance in first 200 cycles.[33] This is ascribed to the strong chemical interaction from the polymeric structure containing P═S bonds in the SPD materials to long-chain lithium polysulfides. This affinity for lithium polysulfides reduces the dissolution in ether-based electrolyte, reducing some of the negative impact of "shuttle effect". While in the region of medium frequency, a semi-ellipse observed in all SPD-based cells is attributed to the solid-electrolyte interphase (SEI) at the Li metal anode resulting from the passivation of the lithium surface, consistant with some results in the EIS studies of lithium metal electrodes in Li ion systems.[48,49] Whereas at low frequencies, the inclined line corresponds to the general Li^+ diffusion process through the SEI film on the lithium metal, electrolyte and the polymeric electrode.[50,51] Intriguingly, a considerable disparity could also be noticed in low frequency region that there is a distinct semi-circle for both SPD1 and SPD3, but not for SPD2. This suggests different electrochemical behaviour between these materials. According to some detailed studies of the EIS spectra in Li–S system, this semi-circle could be ascribed to the irreversible deposition of low-order polysulfides on the cathode. This insulating layer, blocking the electrochemically active surface, is not conductive to the charge transfer process in the following cycles.[50,51] Therefore, the lack of the semi-ellipse in low frequency for SPD2 suggests an improved reversibility of liquid–solid reaction and further sufficient use of active sulfur during cycling, which is beneficial to the capacity retention after long-term test as shown previously.

The morphology of the positive electrodes of SPD1-3 before and after long-term cycling was investigated by SEM (Fig. S22–S24). In terms of the initial disc surface condition among several SPD samples, the electrodes based on both SPD1 (Fig. S22a and b) and SPD3 (Fig. S24a and b) with micrometre size possess similar morphology where polymer bulks particles are surrounded by carbon conductive agents as well as numerous visible cracks.[52] In contrast, benefiting from the comparable size, the electrode containing SPD2 (Fig. S23a and b). exhibits a more uniform surface, as evidenced by smaller image contrast difference, with fewer cracks. Meanwhile, the nanoparticles are evenly mixed within the carbon matrix without severe aggregation. After long-term cell cycling, the morphology of all SPD electrodes change. For SPD1, some deep holes with irregular shape are observed in Fig. S22c, which

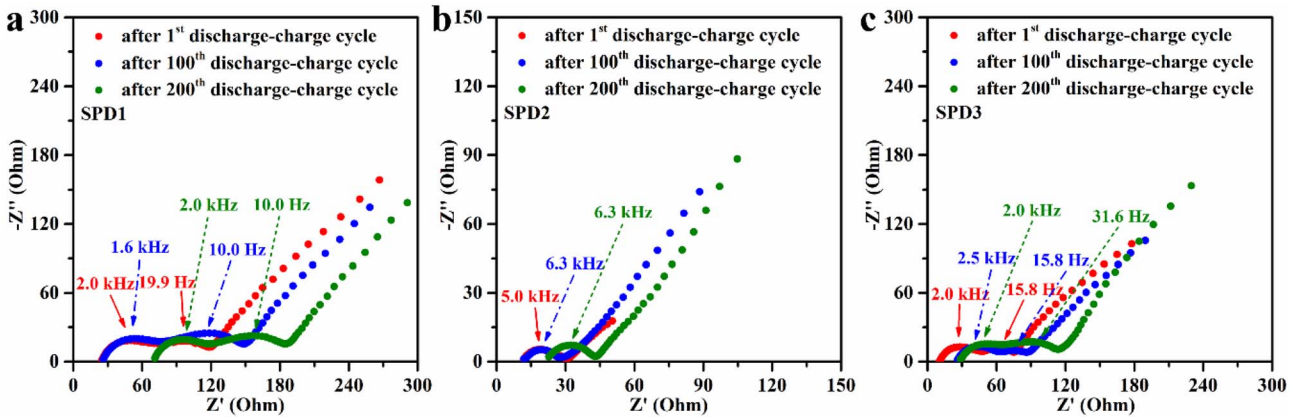

Fig. 5 Nyquist plots under open circuit voltage after the 1st, 100th and 200th discharge–charge cycles of the cells based on (a) SPD1, (b) SPD2 and (c) SPD3.

could suggest dissolution of a soluble fraction during electrochemical cycling. Additionally, newly generated thin layers covering relatively large areas of the surface are visible under high magnification in Fig. S22d. Numerous sulfur species clusters growing after cycling suggests that it is difficult for SPD1 to retain the initial polymeric structure during continuous breaking and reforming of the S–S bonds (Fig. S22e and f). Similar conclusions could be made regarding SPD3 in which two distinct morphologies of new features appear which were not present in the as made electrodes: these new flat solid features are likely to be low-order polysulfides generated during cycling (Fig. S24d), and striated species that are potentially crystalline sulfur generated in charging process (Fig. S24e and f). Both new features overlay the active surface exacerbating roughness of the positive electrode. Interestingly, the SPD2 disc exhibits a notable difference, with only shallow pinholes distributed on the surface and only a much smaller area covered by irreversibly deposited solid polysulfides can be observed (<1 μm) (Fig. S23d). The needle-like structures appearing in Fig. S23 are explained as recrystallised sulfur species formed after long-term cycling.[53,54] The SEM of cycled SPD2 concurs with both the favourable electrochemical performance and EIS data. Furthermore, the sulfur species with a distinct and regular needle-like shape retains good contact with carbon agents after long-term testing (Fig. S23e and f).

Chemical confinement

DFT calculations were conducted to investigate the potential interaction with long-chain polysulfides of the P=S containing functionality. The additional sulfur atom in D4VPP can

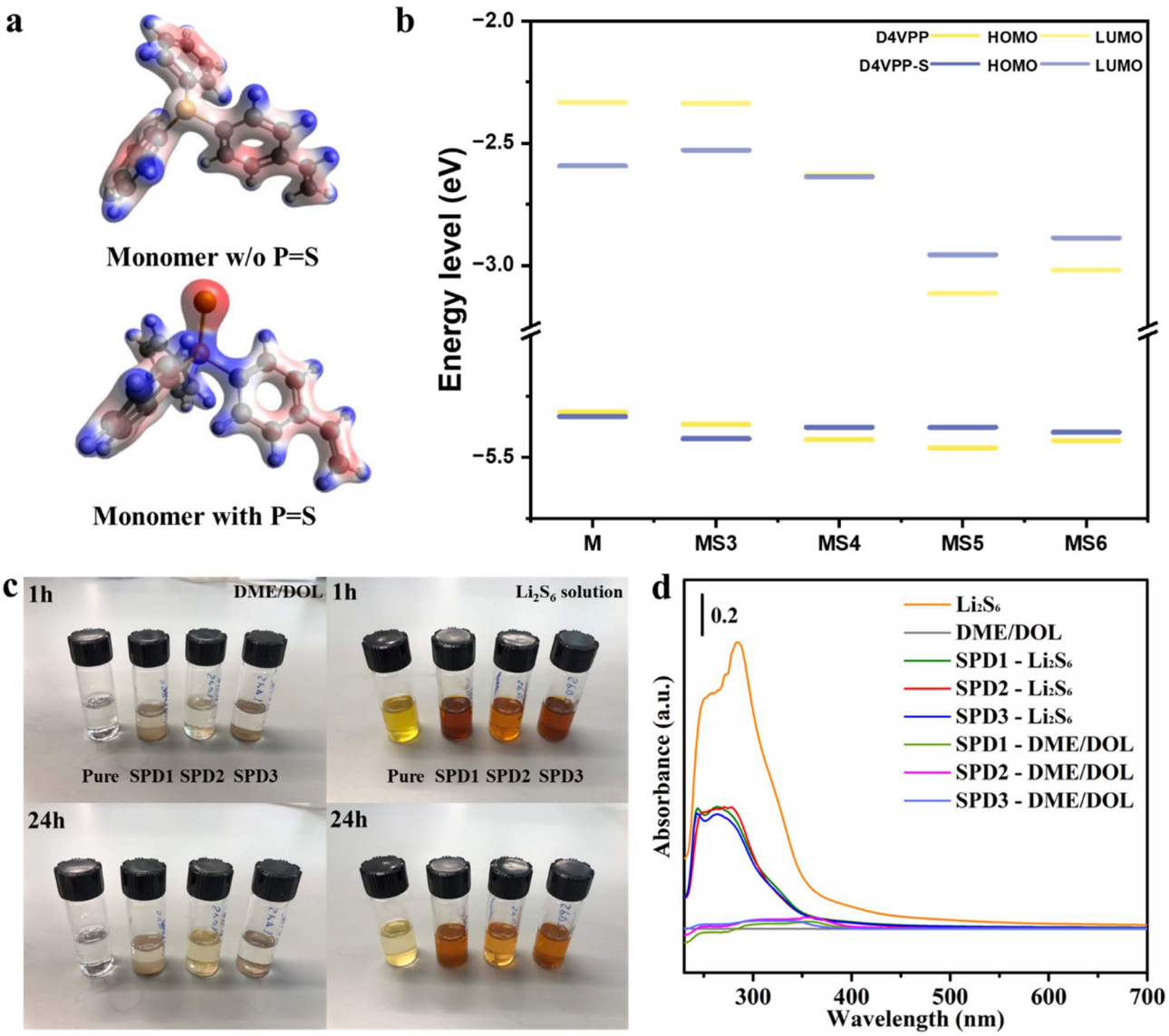

Fig. 6 Chemical confinement investigation of SPD samples. (a) The calculated ESP maps of D4VPP monomers with or without P=S bonds. (b) Calculated HOMO and LUMO energy levels of D4VPP and D4VPP-S under different model structures (c) photographs of SPD1-3 immersed in DME/DOL solvent and Li_2S_6 solution after 1 and 24 hours. (d) UV-vis spectra of DME/DOL solvent and Li_2S_6 solutions before and after SPD powder dispersion.

withdraw electrons from phosphorous, as shown in the 31P NMR spectrum (Fig. 1d), and possibly induce high polarity in the P═S bond. To simplify the calculation of reacted monomer, the computational model is built as the monomer with the C═C bond open and a sulfur loop with different ranks (3–5) attached. For comparison, the highest occupied molecular orbital (HOMO) levels, lowest unoccupied molecular orbital (LUMO) levels and electrostatic potential (ESP) maps for the monomers with or without P═S bond were shown in Fig. 6a, b, S25 and S26, illustrating electron orbital shapes and charge distribution, respectively. The analysis results reveal a distinct difference in the electronic structures between the molecule D4VPP and its sulfurated derivative, D4VPP-S. Specifically, while their HOMO energy levels are comparable, the LUMO energy level of D4VPP-S is lower than that of D4VPP. Furthermore, a systematic decrease in the LUMO energy level of the molecule and its derivatives is observed as the number of sulfur atoms increases. Consequently, the energy gap ($E_g = E_{LUMO} - E_{HOMO}$) gradually narrows with an increasing number of sulfur atoms. D4VPP-S exhibits a smaller energy gap than D4VPP, indicating its higher intrinsic reactivity. According to the ESP results, for initial D4VPP monomer, although a lone pair of electrons is clearly found on P atom and able to keep stable after the saturation of C═C bond. The simulated ESP maps, where red areas demonstrate higher electron density while the blue areas are electron deficient, indicate this P atom possesses relatively weak attractive and repulsive force for positive charges, which suggests its limited contribution to chemically anchoring long-chain polysulfides. Upon introducing a P═S bond, the electrostatic potential distribution of the molecule undergoes a significant change. The incorporated P═S group generates strong polarity, leading to the formation of clear active sites. Regardless of the state of the C═C bond, the S (in P═S bonds) atom consistently exhibits a marked affinity for positive charge, while the P atom remains in an electron-deficient region, serving as an optimal electrophilic site. This is expected to provide active sites in high-order polysulfides during electrochemical processes and could impact on the notorious "shuttle effect" effectively.[55–57]

In addition to the DFT simulation, SPD1-3 were dispersed in 1 mM Li_2S_6 solution for 24 h (Fig. 6c) and UV-vis spectra of the solutions before and after powder dispersion were measured to experimentally evaluate the chemical anchor effect of SPD polymers to long-chain polysulfides *via* the intensity disparity of characteristic adsorption bands. In Fig. 6d, the weak adsorption band in the range of 395–280 nm could be observed from DME/DOL solvent after powder dispersion, indicating the relatively small solubility of SPD polymers in solvent. While for the untreated Li_2S_6 solution, there are two obvious adsorption bands from 500–370 nm, corresponding to LiS_6^-, and from 350–230 nm, corresponding to Li_2S_6.[58] After adding SPD polymers in the solution, the intensity of both adsorption bands dramatically decreases, implying the effective anchor effect towards long-chain polysulfides from SPD polymers. Given that the limited chemical confinement from DCPD monomer in our previous results,[33] the main contribution could therefore be attributed to D4VPP-based polymeric backbone with P═S bonds. Therein, the colour of all dried samples turned dark red, proving the sufficient adsorption of long-chain polysulfides (Fig. S27). Overall, the combination of computational and experimental results implies a chemical affinity to high order polysulfides from the backbone of SPD samples, mostly contributed by the sulfur in P═S bonds.

Conclusion

Ternary sulfur – diphenyl(4-vinylphenyl) phosphine – dicyclopentadiene (SPD) polymeric nanoparticles with homogenous size around 80 nm were successfully prepared by inverse vulcanisation and anti-solvent precipitation methods. NMR characterisation of the designed model compounds confirms that the phosphorous heteroatoms bonded to three branches are sulfurised to form P═S bonds during synthesis. The P═S groups provide a strong chemical affinity to lithium ions in high-order polysulfide intermediates, evidenced by DFT calculation and experimental measurements. The 80 nm particle size SPD polymer (denoted at SPD2) demonstrated a specific capacity of 1436 mAh g_s^{-1} under 0.05C and capacity retention during cycling of 0.046% reduction per cycle at 0.5C over 500 cycles which greatly outperformed the micron scale samples (denoted as SPD1 and SPD3). The improved performance of the 80 nm SPD polymers is attributed to the higher degree of active sulfur fraction derived from the greater accessibility of the uniform nanoparticulate morphology, as well as the formation of an effective electronic network arising from improved interfacial contact between the carbon black conductive additive and the active sulfur species. This study highlights the importance of not just the sulfur polymer chemical structure, but also how the materials are formulated during electrode preparation.

Conflicts of interest

The authors declare no conflict of interest.

Data availability

The data supporting this article have been included as part of the supplementary information (SI). Supplementary information is available. See DOI: https://doi.org/10.1039/d6se00065g.

Acknowledgements

H. W. and P. Y thank the China Scholarship Council (CSC) for awarding them a scholarship and the Materials Innovation Factory (MIF) team members for their support in operating instruments. L. J. H. and A. R. N. acknowledge the EPSRC funding under grant EP/R020744/1 and financial support from the Faraday Institution CATMAT (EP/S003053/1, FIRG016) and H. W. acknowledges X. Lin, H. Cai and J. Lim for experimental help and useful discussion. T. H. was supported by a Royal Society University Research Fellowship.

References

1 P. G. Bruce, S. A. Freunberger, L. J. Hardwick and J. M. Tarascon, *Nat. Mater.*, 2012, **11**, 19.
2 P. G. Bruce, L. J. Hardwick and K. M. Abraham, *MRS Bull.*, 2011, **36**, 506.
3 Q. Pang, X. Liang, C. Y. Kwok and L. F. Nazar, *Nat. Energy*, 2016, **1**, 16132.
4 S. Chung, C. Chang and A. Manthiram, *Adv. Funct. Mater.*, 2018, **28**, 1801188.
5 Y. V. Mikhaylik and J. R. Akridge, *J. Electrochem. Soc.*, 2004, **151**, A1969.
6 C. Yang, Y. Yin, Y. Guo and L. Wan, *J. Am. Chem. Soc.*, 2015, **137**, 2215.
7 S. Rehman, S. Guo and Y. Hou, *Adv. Mater.*, 2016, **28**, 3167.
8 J. Song, M. L. Gordin, T. Xu, S. Chen, Z. Yu, H. Sohn, J. Lu, Y. Ren, Y. Duan and D. Wang, *Angew. Chem., Int. Ed.*, 2015, **54**, 4325.
9 Y. Zhong, D. Chao, S. Deng, J. Zhan, R. Fang, Y. Xia, Y. Wang, X. Wang, X. Xia and J. Tu, *Adv. Funct. Mater.*, 2018, **28**, 1706391.
10 L. Peng, Z. Wei, C. Wan, J. Li, Z. Chen, D. Zhu, D. Baumann, H. Liu, C. S. Allen, X. Xu, A. I. Kirkland, I. Shakir, Z. Almutairi, S. Tolbert, B. Dunn, Y. Huang, P. Sautet and X. Duan, *Nat. Catal.*, 2020, **3**, 762.
11 W. Hua, T. Shang, H. Li, Y. Sun, Y. Guo, J. Xia, C. Geng, Z. Hu, L. Peng, Z. Han, C. Zhang, W. Lv and Y. Wan, *Nat. Catal.*, 2023, **6**, 174.
12 W. J. Chung, J. J. Griebel, E. T. Kim, H. Yoon, A. G. Simmonds, H. J. Ji, P. T. Dirlam, R. S. Glass, J. J. Wie, N. A. Nguyen, B. W. Guralnick, J. Park, Á. Somogyi, P. Theato, M. E. Mackay, Y. E. Sung, K. Char and J. Pyun, *Nat. Chem.*, 2013, **5**, 518.
13 F. Zhao, Y. Li and W. Feng, *Small Methods*, 2018, **2**, 1800156.
14 H. Kang, H. Kim and M. J. Park, *Adv. Energy Mater.*, 2018, **8**, 1802423.
15 B. Oschmann, J. Park, C. Kim, K. Char, Y. E. Sung and R. Zentel, *Chem. Mater.*, 2015, **27**, 7011.
16 J. Kim, A. Elabd, S. Y. Chung, A. Coskun and J. W. Choi, *Chem. Mater.*, 2020, **32**, 4185.
17 B. Zhang, S. Petcher, R. A. Dop, P. Yan, W. Zhao, H. Wang, L. J. Dodd, T. O. McDonald and T. Hasell, *J. Mater. Chem. A*, 2022, **10**, 13704.
18 F. Uebel, W. Wei, M. Remmers and H. Thérien-Aubin, *Chem. Commun.*, 2022, **58**, 12959.
19 J. A. Smith, S. J. Green, S. Petcher, D. J. Parker, B. Zhang, M. J. H. Worthington, X. Wu, C. A. Kelly, T. Baker, C. T. Gibson, J. A. Campbell, D. A. Lewis, M. J. Jenkins, H. Willcock, J. M. Chalker and T. Hasell, *Chem.–A Eur. J.*, 2019, **25**, 10433.
20 T. Chen, S. Zhang, L. Hua, Z. Xu, L. Zhou and J. Wang, *Macromol. Res.*, 2019, **27**, 931.
21 D. J. Parker, H. A. Jones, S. Petcher, L. Cervini, J. M. Griffin, R. Akhtar and T. Hasell, *J. Mater. Chem. A*, 2017, **5**, 11682.
22 N. D. Knöfel, H. Rothfuss, P. Tzvetkova, B. Kulendran, C. Barner-Kowollik and P. W. Roesky, *Chem. Sci.*, 2020, **11**, 10331.
23 K. J. Sykes, S. Harrisson and D. J. Keddie, *Macromol. Chem. Phys.*, 2016, **217**, 2310.
24 P. H. Maag, F. Feist, H. Frisch, P. W. Roesky and C. Barner-Kowollik, *Macromolecules*, 2022, **55**, 9918–9924.
25 A. Kusumaatmaja, T. Ando, K. Terada, S. Hirohara, T. Nakashima, T. Kawai, T. Terashima and M. Tanihara, *J. Polym. Sci., Part A: Polym. Chem.*, 2013, **51**, 2527–2535.
26 A. R. Schultz, G. B. Fahs, C. Jangu, M. Chen, R. B. Moore and T. E. Long, *Chem. Commun.*, 2016, **52**, 950.
27 W. Jiang, J. Li, M. Wu, L. He, G. Zhou and Z. Wang, *Fuel*, 2023, **338**, 127291.
28 M. Y. Omeir, V. S. Wadi and S. M. Alhassan, *Mater. Lett.*, 2020, **259**, 126887.
29 H. Tao, S. Du, F. Zhang, L. Xiong, Y. Zhang, H. Ma and X. Yang, *ACS Appl. Mater. Interfaces*, 2018, **10**, 34245.
30 F. Zhang, J. Dai, A. Wang and W. Wu, *Inorganica Chim. Acta*, 2017, **466**, 333.
31 I. Palmová, J. Kosek, J. Schöngut, M. Marek and K. Štěpánek, *Chem. Eng. Sci.*, 2001, **56**, 927.
32 Z. Yao, X. Xu, Y. Dong, X. Liu, B. Yuan, K. Wang, K. Cao and G. Luo, *Chem. Eng. Sci.*, 2020, **228**, 115892.
33 H. Wang, B. Zhang, R. Dop, P. Yan, A. R. Neale, L. J. Hardwick and T. Hasell, *J. Power Sources*, 2022, **545**, 231921.
34 A. Rafie, R. Pereira, A. A. Shamsabadi and V. Kalra, *J. Phys. Chem. C*, 2022, **126**, 12327.
35 X. Zhang, K. Chen, Z. Sun, G. Hu, R. Xiao, H. M. Cheng and F. Li, *Energy Environ. Sci.*, 2020, **13**, 1076.
36 C. W. Schmitt, L. J. Dodd, J. K. Walz, L. Deterding, P. Lott, A. P. Grimm, M. P. Shaver, T. Hasell and P. Théato, *RSC Sustain.*, 2025, **3**, 4190–4227.
37 J. J. Griebel, G. Li, R. S. Glass, K. Char and J. Pyun, *J. Polym. Sci., Part A: Polym. Chem.*, 2015, **53**, 173–177.
38 J. Chalker, M. Mann, M. Worthington and L. Esdaile, *Org. Mater.*, 2021, **3**, 362–373.
39 G. Hu, Z. Sun, C. Shi, R. Fang, J. Chen, P. Hou, C. Liu, H. M. Cheng and F. Li, *Adv. Mater.*, 2017, **29**, 1603835.
40 A. Hoefling, D. T. Nguyen, P. Partovi-Azar, D. Sebastiani, P. Theato, S. W. Song and Y. J. Lee, *Chem. Mater.*, 2018, **30**, 2915.
41 C. Zhang, R. Du, J. J. Biendicho, M. Yi, K. Xiao, D. Yang, T. Zhang, X. Wang, J. Arbiol, J. Llorca, Y. Zhou, J. R. Morante and A. Cabot, *Adv. Energy Mater.*, 2021, **11**, 2100432.
42 M. Du, P. Geng, C. Pei, X. Jiang, Y. Shan, W. Hu, L. Ni and H. Pang, *Angew. Chem., Int. Ed.*, 2022, **61**, e202209350.
43 R. Chu, T. T. Nguyen, Y. Bai, N. H. Kim and J. H. Lee, *Adv. Energy Mater.*, 2022, **12**, 2102805.
44 J. Lee and W. Choi, *J. Electrochem. Soc.*, 2015, **162**, A935.
45 G. Zheng, Q. Zhang, J. J. Cha, Y. Yang, W. Li, Z. W. Seh and Y. Cui, *Nano Lett.*, 2013, **13**, 1265–1270.
46 X. B. Cheng, H. J. Peng, J. Q. Huang, R. Zhang, C. Z. Zhao and Q. Zhang, *ACS Nano*, 2015, **9**, 6373.
47 Y. Fu and A. Manthiram, *Chem. Mater.*, 2012, **24**, 3081.
48 S. Drvarič Talian, J. Bobnar, A. R. Sinigoj, I. Humar and M. Gaberšček, *J. Phys. Chem. C*, 2019, **123**, 27997.
49 J. Song, *J. Power Sources*, 2002, **111**, 255.

50 J. Fang, W. Shen, S. H. S. Cheng, S. Ghashghaie, H. K. Shahzad and C. Y. Chung, *J. Power Sources*, 2019, **441**, 227202.
51 S. Waluś, C. Barchasz, R. Bouchet and F. Alloin, *Electrochim. Acta*, 2020, **359**, 136944.
52 Y. S. Zhang, N. E. Courtier, Z. Zhang, K. Liu, J. J. Bailey, A. M. Boyce, G. Richardson, P. R. Shearing, E. Kendrick and D. J. L. Brett, *Adv. Energy Mater.*, 2022, **12**, 2102233.
53 S. Waluś, C. Barchasz, J.-F. Colin, J.-F. Martin, E. Elkaïm, J.-C. Leprêtre and F. Alloin, *Chem. Commun.*, 2013, **49**, 7899–7901.
54 F. Liu, W. Lu, J. Huang, V. Pimenta, S. Boles, R. Demir-Cakan and J.-M. Tarascon, *Nat. Commun.*, 2023, **14**, 7350.
55 J. Xu, S. An, X. Song, Y. Cao, N. Wang, X. Qiu, Y. Zhang, J. Chen, X. Duan, J. Huang, W. Li and Y. Wang, *Adv. Mater.*, 2021, **33**, 2105178.
56 Z. Chen, H. Cui, Y. Hou, X. Wang, X. Jin, A. Chen, Q. Yang, D. Wang, Z. Huang and C. Zhi, *Chem*, 2022, **8**, 2204.
57 J. Zhao, G. Yan, X. Zhang, Y. Feng, N. Li, J. Shi and X. Qu, *Chem.–Eng. J.*, 2022, **442**, 136352.
58 B. Zhang, J. Wu, J. Gu, S. Li, T. Yan and X. Gao, *ACS Energy Lett.*, 2021, **6**, 537.

